

**OPEN ACCESS**

## Multistep Improvement of Pilot-Scale 21700 Cells for Increased Fast-Charging Capability: Combining Optimized Electrolyte, Cell Design and Fast-Charging Protocol

To cite this article: Christin Hogrefe *et al* 2023 *J. Electrochem. Soc.* **170** 110535

View the [article online](#) for updates and enhancements.

### You may also like

- [Energy Density of Cylindrical Li-Ion Cells: A Comparison of Commercial 18650 to the 21700 Cells](#)

Jason B. Quinn, Thomas Waldmann, Karsten Richter *et al.*

- [Multi-resolution simulation of focused ultrasound propagation through ovine skull from a single-element transducer](#)

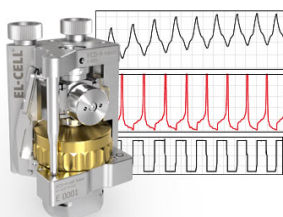
Kyungho Yoon, Wonhye Lee, Phillip Croce *et al.*

- [Signatures of Inflow Motion in Cores of Massive Star Formation: Potential Collapse Candidates](#)

Yuefang Wu, Christian Henkel, Rui Xue *et al.*

### Measure the Electrode Expansion in the Nanometer Range. Discover the new ECD-4-nano!

  
electrochemical test equipment




- Battery Test Cell for Dilatometric Analysis (Expansion of Electrodes)
- Capacitive Displacement Sensor (Range 250  $\mu\text{m}$ , Resolution  $\leq 5$  nm)
- Detect Thickness Changes of the Individual Electrode or the Full Cell.

[www.el-cell.com](http://www.el-cell.com) +49 40 79012-734 [sales@el-cell.com](mailto:sales@el-cell.com)





# Multistep Improvement of Pilot-Scale 21700 Cells for Increased Fast-Charging Capability: Combining Optimized Electrolyte, Cell Design and Fast-Charging Protocol

Christin Hogrefe,<sup>1</sup> Markus Hölzle,<sup>1</sup> Margret Wohlfahrt-Mehrens,<sup>1,2</sup> and Thomas Waldmann<sup>1,2,z</sup> 

<sup>1</sup>ZSW - Zentrum für Sonnenenergie- und Wasserstoff-Forschung Baden-Württemberg, D-89081 Ulm, Germany

<sup>2</sup>HIU - Helmholtz Institute Ulm for Electrochemical Energy Storage, 89081 Ulm, Germany

In this publication, different cell- and charging parameters (advanced fast-charging protocol, 21700 tab design, electrolyte composition) are changed in a systematic step-by-step approach to reduce charging time while keeping the anode and cathode cell chemistry and electrodes (graphite—NMC 622 full cell) unchanged. Preliminary tests were carried out using 3-electrode full cells with a Li metal reference electrode to identify charging conditions that avoid Li metal deposition. In addition, the effects of the anode potential are investigated in 3-electrode full cells with a Li metal reference electrode. The optimized charging protocols from the 3-electrode full cells were then transferred to 2-electrode pilot-scale 21700 full cells. Two different tab designs (1 × 1 welded tabs and 120 × 125 foil tabs) were used in these cells. To improve the charging time further, an electrolyte with higher ionic conductivity was used under the best conditions from the previous tests. Cross-sectional *in situ* optical microscopy was used to visualize the transport effects within the anode. In the optimized 21700 cell (advanced fast-charging, 120 × 125 foil tabs, better Li<sup>+</sup> transport in the electrolyte), the synergistic effects of the three different optimization steps reduced the charging time to 80% SOC by 46% compared to the baseline cell.

© 2023 The Author(s). Published on behalf of The Electrochemical Society by IOP Publishing Limited. This is an open access article distributed under the terms of the Creative Commons Attribution 4.0 License (CC BY, <http://creativecommons.org/licenses/by/4.0/>), which permits unrestricted reuse of the work in any medium, provided the original work is properly cited. [DOI: 10.1149/1945-7111/ad0c65]



Manuscript submitted August 8, 2023; revised manuscript received October 5, 2023. Published November 27, 2023. *This paper is part of the JES Focus Issue on Journey of Lithium-Ion: Performance, Safety, and Lifespan.*

Supplementary material for this article is available [online](#)

With the rapid increase of the number of battery electric vehicles (BEV), there is also a growing demand for (fast-)charging infrastructure.<sup>1</sup> The target time to charge a battery to 80% state-of-charge (SOC, of a usable energy density of 550 Wh l<sup>-1</sup>) is less than 15 min in order to meet the needs of BEVs on long-distance traveling as well as keeping the number of charging stations at an acceptable level.<sup>2</sup>

However, fast-charging has many challenges.<sup>3</sup> High C-rates applied to a battery during charging result in high overvoltages. The cell voltage  $U$  of a battery is defined as the sum of the equilibrium, standard Voltage  $\Delta E_0$  and the overvoltages of anode  $\eta_{anode}$  and cathode  $\eta_{cathode}$ :<sup>3,4</sup>

$$U = \Delta E_0 + \eta_{anode} + \eta_{cathode} \quad [1]$$

The overvoltage  $\eta$  is defined as the sum of the Ohmic overvoltage  $\eta_{ohm}$ , the kinetic overvoltage  $\eta_{kinetic}$ , and the mass-transport overvoltage  $\eta_{mass-transfer}$ :<sup>4</sup>

$$\eta = \eta_{ohm} + \eta_{kinetic} + \eta_{mass-transfer} \quad [2]$$

The Ohmic overvoltage is caused by the so-called  $IR$ -drop, which follows Ohm's law.<sup>4</sup>  $R$  represents the resistance of the cell (including all cell components).<sup>4</sup> For example, by increasing the electrode areas, the Ohmic resistance can be reduced.<sup>5</sup>

The kinetic overpotential is mainly driven by the charge-transfer kinetics at the active material surface and can be described quantitatively by the Butler-Volmer equation.<sup>3,4</sup> However, surface films such as the solid-electrolyte-interphase (SEI) and cathode-electrolyte-interphase (CEI) must be considered since they can drastically affect the charge-transfer kinetics.<sup>3,6</sup>

The main contributors to the mass transport are the ion transport of Li<sup>+</sup> through the electrode's pores (migration) and within the active material particles (solid-diffusion).<sup>3,7-9</sup> The electrode microstructure and pore system are influenced by many parameters, such

as the size distribution and shape of the active material particles, conductive additives, and applied binder.<sup>7-9</sup> The ionic pathways through the porous electrode are described by its tortuosity.<sup>10-12</sup> Especially at higher charging rates, the transport properties can cause a depletion of Li<sup>+</sup> in the electrolyte within the parts of the electrode close to the current collector.<sup>8,9</sup> This causes an inhomogeneous lithiation distribution within the electrodes<sup>13,14</sup> which can ultimately lead to faster aging at the electrode surface.<sup>15</sup> Changing the conductive salt concentration<sup>8,16</sup> or the conductive salt itself<sup>17</sup> can improve the mass transport properties and allow higher charging rates.

In Li-ion full cells, the anode was found to be the rate limiting electrode during fast-charging.<sup>18</sup> The anode potential easily drops below 0 V vs Li/Li<sup>+</sup> at high charging C-rates, where Li metal deposition becomes thermodynamically possible.<sup>3,4,19-21</sup> However, Li metal deposition is known to be a large contributor to the irreversible loss of battery capacity as well as critical for battery safety.<sup>3,21-23</sup>

When larger format cells, such as prismatic or cylindrical cells, are used for fast-charging, high currents lead to self-heating of the cells driven by the Ohmic resistance.<sup>5,24,25</sup> Although higher temperatures are overall beneficial regarding charging kinetics, cells exposed to high temperatures for prolonged time periods are aging faster.<sup>21</sup> Changes in the tab design of larger format cells can counter such heating.<sup>25-27</sup> Frank et al.<sup>25</sup> investigated the effect of foil tabs (tabs made from the electrode's metal foils, also called "tabless design") on the performance of different cylindrical cells (18650, 21700, 46800 design) in comparison to segmented tab design by simulations. They found both a decrease in anode polarization as well as a lower average cell temperature during charging.<sup>25</sup> Sturm et al.<sup>24</sup> found in their simulations that cylindrical cells (18650, 21700, 26650 design) with a larger number of tabs have a higher fast-charging capability. Our group<sup>26,27</sup> demonstrated experimentally an increased cycle life in cylindrical 21700 cells, by changing the welded tab design with only a few single tabs to a foil tab design.

Using advanced charging strategies is another way to reduce the charging time. By changing the charging protocol from the typically used constant-current (CC)—constant-voltage (CV) charging to alternative

<sup>z</sup>E-mail: [thomas.waldmann@zsw-bw.de](mailto:thomas.waldmann@zsw-bw.de)

charging procedures, the charging time can be reduced.<sup>24,28–34</sup> Already in the late 1990s' and early 2000s', Ikeya et al.<sup>28,29</sup> demonstrated the advantages of multistage constant current (MS-CC) charging on battery charging capabilities of lead acid batteries<sup>28</sup> and Ni-MH<sup>29</sup> batteries. In the early 2000s, Notten et al.<sup>35</sup> proposed boost-charging for Li-ion batteries, where charging time is markedly reduced by a CV-CC-CV and 2-step-CCCV charging protocols. Since then, many different charging strategies<sup>36</sup> have been proposed over the years such as pulse charging,<sup>37–39</sup> constant-power (CP),<sup>31,37</sup> MS-CC(CV),<sup>24,25,30–33,40–43</sup> and current profiles.<sup>32</sup> All these examples show that the charging strategy is highly dependent on the transport parameters of the cell and have to be tested for each cell chemistry individually.

We would like to point out that there is a lack of knowledge in literature regarding the interaction of individual improvements on the overall performance on cell level. For example, it is not clear until now if single improvements interfere with each other, resulting in trade-offs, or even positively support each other, resulting in synergistic effects.

In this paper, we investigated 21700 cells with known cell chemistry manufactured in our pilot line to study the effect of (1) charging-protocol, (2) cylindrical cell tab design, and (3) electrolyte composition on the fast-charging capability. To the best of our knowledge, this is the first report on such a combination of single improvements for 21700 cells. The aim of this study is finding the influences of these parameters and their combination, excluding the effects of electrodes or the cell chemistry.

The advanced multistage - constant current constant voltage (MS-CCCV) charging protocol is determined in small 3-electrode PAT full cells and transferred to 21700 cells. First (1), we discuss the effect of the anode potential and the charging protocol in 3-electrode PAT full cells. Second (2), two tab designs in 21700 cells (1 × 1 welded and 120 × 125 foil tabs) are directly compared using both 1 C and advanced MS-CCCV charging. Third (3), the electrolyte is changed to one with higher ionic conductivity. Due to the changed ionic transport properties, another MS-CCCV protocol is determined in accordance with step (1) and then tested in the best 21700 cell design determined in step (2). The effect of the higher ionic conductivity on the charge distribution within the anode was visualized by cross-sectional in situ optical microscopy. Last, 21700 cells with the two cell designs, two charging protocols (1 C CCCV and MS-CCCV), and the two electrolytes were aged, testing the effect of the faster charging on the cycling aging behavior. Finally, the overall performance in terms of cell impedance (at 1 kHz), charging time and aging rate of the optimized 21700 cells are compared to the initial 21700 cell design. The effects of cell design, self-heating of cells, electrolyte composition, aging, as well as further optimization steps are discussed in detail.

## Experimental

**Cell chemistry.**—In all experiments, a graphite (SMG-A5, Hitachi) anode (2.7 mAh cm<sup>-2</sup> at 0.1 C, electrode thickness (double side coated): 133 μm) and a NMC 622 (BASF) cathode (2.37 mAh cm<sup>-2</sup> at 0.1 C, electrode thickness (double side coated):

117 μm) with a N/P ratio of 1.14 were used. The same electrodes were used in previous studies from our group and were manufactured at ZSW's research production line.<sup>5,26,27</sup> It must be noted that the electrodes had not been optimized for fast-charging.

Two different electrolyte solutions (Gotion) were used: 1.0 M LiPF<sub>6</sub> in EC:EMC (3:7 wt) + 2 wt. % VC and 1.4 M LiPF<sub>6</sub> in EC:DEC (3:7 wt) + 2 wt. % VC. In this paper, these electrolytes will be referred to as electrolyte I and electrolyte II, respectively.

The ionic conductivity of electrolyte I (9 mS cm<sup>-1</sup> at 25 °C) and electrolyte II (12 mS cm<sup>-1</sup> at 25 °C) was determined by electrochemical impedance spectroscopy (Amplitude: 10 mV, Frequency: 100 kHz—1 Hz) using a HC microcell (Serie 357–03, rhd-instruments).

**3-electrode full cells.**—In order to optimize the charging procedure, 3-electrode PAT full cells (EL-Cell GmbH with ring Li reference) were assembled at ZSW. Anode and cathode with 18 mm diameter were used in these cells, as well as one layer of glass fiber separator (GF/A, Whatman, 260 μm thickness) and 150 μl electrolyte solution. Table I gives an overview of all assembled 3-electrode PAT full cells in this study. Before assembly, the electrodes were dried at 130 °C, the separator at 230 °C, and the cell housing at 60 °C under vacuum conditions overnight. The reference value for setting the C-rates was the cell capacity after formation for each individual cell (mean value of all cells: 2.44 mAh cm<sup>-2</sup> ± 0.1 mAh cm<sup>-2</sup>).

**21700 cells.**—Table II provides an overview of the cylindrical 21700 cell configurations, which were manufactured at ZSW's pilot-line. Two different tab designs were investigated in this study. The 1 × 1 welded tab design from Refs. 26, 27 as well as a 120 × 125 foil multi-tab design, similar to the 101 × 125 from Ref. 27, were used. All 21700 cells utilized a 2325 Celgard separator (Celgard, 25 μm thickness) and 6 ml of electrolyte. All cells had been designed to the same theoretical capacity of 2.5 Ah, which was used as reference value to set the C-rates. The cell assembly process was already described in our previous papers.<sup>26,27</sup> The assembly of the cells was conducted in different batches. After filling the electrolyte, the cell impedance was measured using a Hioki BATTERY HiTESTER 3554 at a frequency of 1 kHz ± 30 Hz (Z at 1 kHz).

**Electrochemical testing.**—All electrochemical tests were performed at ZSW using BaSyTec CTS and XCTS cycling units. Pre-tests in 3-electrode PAT full cells were conducted at room temperature. Tests in cylindrical 21700 cells were conducted in Vötsch climate chambers at 25 °C.

Before formation, all cells rested for 20 h. Three times for formation, the cells were charged with a constant current of 0.1 C to 4.2 V and with a constant voltage until 0.05 C was reached, and then discharged with a rate of 0.1 C to 2.7 V. The third discharge capacity of the formation was used as a reference value for 100% SOC. Afterwards, the 21700 cells were charged with 0.2 C until a capacity of 1 Ah was reached.

**Table I. Overview on 3-electrode PAT full cell measurement configurations, testing, and reproduction. The labels refer to the electrochemical test and the electrolyte used (I: 1.0 M LiPF<sub>6</sub> in EC:EMC (3:7 wt) + 2 wt. % VC and II: 1.4 M LiPF<sub>6</sub> in EC:DEC (3:7 wt) + 2 wt. % VC).**

Label	Electrochemical testing	Electrolyte	Number of cells cycled
EL-CR-I	Charge Rate Capability	1.0 M LiPF <sub>6</sub> in EC:EMC (3:7 wt) + 2 wt. % VC	4
EL-CR-II	Charge Rate Capability	1.4 M LiPF <sub>6</sub> in EC:DEC (3:7 wt) + 2 wt. % VC	4
EL-3C-I	MS-CC: Starting Rate 3 C	1.0 M LiPF <sub>6</sub> in EC:EMC (3:7 wt) + 2 wt. % VC	3
EL-4C-I	MS-CC: Starting Rate 4 C	1.0 M LiPF <sub>6</sub> in EC:EMC (3:7 wt) + 2 wt. % VC	3
EL-4C-II	MS-CC: Starting Rate 4 C	1.4 M LiPF <sub>6</sub> in EC:DEC (3:7 wt) + 2 wt. % VC	3
EL-6C-I	MS-CC: Starting Rate 6 C	1.0 M LiPF <sub>6</sub> in EC:EMC (3:7 wt) + 2 wt. % VC	2
EL-CCCV-I	Advanced MS-CCCV	1.0 M LiPF <sub>6</sub> in EC:EMC (3:7 wt) + 2 wt. % VC	2
EL-CCCV-II	Advanced MS-CCCV	1.4 M LiPF <sub>6</sub> in EC:DEC (3:7 wt) + 2 wt. % VC	3

**Table II. Overview of the 21700 cylindrical cell design. The labels refer to the used tab designs (A: 1 × 1 welded tabs and B: 120 × 125 foil tabs) and the used electrolyte solution (I: 1.0 M LiPF<sub>6</sub> in EC:EMC (3:7 wt) + 2 wt. % VC and II: 1.4 M LiPF<sub>6</sub> in EC:DEC (3:7 wt) + 2 wt. % VC).**

Cell type	Tab design	Electrolyte	Mean Z at 1 kHz after electrolyte filling	Number of cells cycled 1 C CCCV	Number of cells cycled advanced MS-CCCV
A-I	1 × 1 welded	1.0 M LiPF <sub>6</sub> in EC:EMC (3:7 wt) + 2 wt. % VC	32.55 mΩ ± 0.55 mΩ @ 0.25 V	2	2
B-I	120 × 125 foil	1.0 M LiPF <sub>6</sub> in EC:EMC (3:7 wt) + 2 wt. % VC	10.85 mΩ ± 0.45 mΩ @ 0.24 V	2	2
B-II	120 × 125 foil	1.4 M LiPF <sub>6</sub> in EC:DEC (3:7 wt) + 2 wt. % VC	9.45 mΩ ± 0.13 mΩ @ 0.21 V	—	2

For the charge-rate capability test in 3-electrode PAT-cells, the cells were charged three times per individual C-rate (0.1 C, 0.5 C, 1 C, 2 C, 3 C, 4 C, and 0.1 C) and rested for 3 h after each charging step. The cells were discharged to 2.7 V with 1 C after each charging step.

To develop multistage charging protocols for the avoidance of Li metal deposition, an approach similar to that of Shkrob et al.<sup>42</sup> was used. The starting C-rate was set to either 3 C, 4 C, or 6 C. The C-rate was gradually reduced in 0.25 C steps when the anode potential reached +10 mV vs Li/Li<sup>+</sup> or the cell voltage reached the cut-off voltage of 4.2 V. The last step included a CV step at 4.2 V, which ended when the current dropped to a C-rate of 0.05 C. In order to apply the multistage charging protocols in cells without an internal Li metal reference electrode, the resulting cell voltage cut-offs for each rate were analyzed and transferred into an advanced 3-step multistage-CCCV (MS-CCCV) protocol (see Table III). Afterwards, the cells were discharged with a C-rate of 0.3 C.

The 21700 cells were aged using different procedures. Before aging, one 1 C CCCV charge and one advanced MS-CCCV charge were recorded of the unaged cells in order to compare the different procedures in the individual 21700 cells directly. For cell type A-I and B-I, two cells were aged by 1 C CCCV charge, the CV phase was stopped when the current dropped to 0.1 C. Every 50 cycles, a check-up cycle was integrated into the aging procedure. In the check-up cycles, the cells were charged with a rate of 1 C. In the beginning of discharge, a 1 A discharge pulse (10 s) followed by a 10 A discharge pulse (1 s) was applied in order to measure the direct current internal resistance (DCIR). Then the cells were discharged at 0.2 C. The analysis of the DCIR values was performed in accordance with Radloff et al.<sup>44</sup> Except of the check-up cycles, the discharge rate was 1 C in all cycling procedures for the 21700 cells.

During cycling of the cylindrical cells, the NTC-type temperature sensor (sensitivity:  $\pm 1$  °C), included in the BaSyTec cycling unit, was taped in the middle-height of the cell cylinders in order to track the surface temperature of the 21700 cells.

**Cross-sectional in situ optical microscopy.**—For visualization of the Li<sup>+</sup> transport in the electrolyte solutions I and II, cross-sectional in situ optical microscopy measurements were performed at ZSW. The in situ cell set-up and preparation of the cross-sectional cell were developed in our group and are described in detail in our previous publications.<sup>13,14</sup> For these measurements, the anode and cathode had identical dimensions (diameter: 16 mm), and two layers of Celgard 2325 separator (diameter: 18 mm) were used. The electrodes were dried overnight under vacuum conditions at 130 °C, and the separator was dried at 70 °C. After assembly, the whole cell was dried at 80 °C for 16 h in a vacuum oven. The cells were first filled with 100  $\mu$ l of electrolyte and additional with 50  $\mu$ l of electrolyte after two hours. Then the cells were pre-charged for 60 s with 0.1 C. 10 h after the initial electrolyte filling, the in situ cells were charged once with 0.1 C to 4.2 V and were held at 4.2 V until the current dropped to 0.05 C. Afterwards, the in situ cells were discharged to 2.7 V with a C-rate of 0.1 C. In the second cycle, the cells were charged with 0.75 C to 4.2 V and were held at 4.2 V until the current dropped to a rate of 0.05 C. Then the cells were discharged to 2.7 V with a rate of 0.75 C. The C-rates were determined by weighing the cut-off of the electrodes and calculating the remaining cathode mass. Then the theoretical capacity was determined using the areal capacity of 2.37 mAh cm<sup>-2</sup>. Two cells were tested for each electrolyte solution.

One stacked image was recorded every 60 s by the custom made digital microscope (PreciPoint), using the 40X objective of the microscope. The stacked images were collected by recording 150 images in 0.25  $\mu$ m distance and merging them using the microscope software. For better visibility of the colored lithiated graphite phases, contrast and color intensity are enhanced in both video and image data. To determine the scale bars, pixel values are divided by 5.33 px  $\mu$ m<sup>-1</sup>.

**General aspects of stepwise optimization.**—Figure 1 schematically shows which parameters were optimized in order to minimize the charging time to 80% SOC. Firstly (1), an advanced MS-CCCV charging protocol is determined in three electrode PAT-EL full cells (Figs. 1a, 1b). In step (2) (Fig. 1c), the resulting advanced MS-CCCV charging protocol is transferred to the 2-electrode 21700 full cell format and tested in two different tab designs (1  $\times$  1 welded tabs and 120  $\times$  125 foil tabs). Last (3), an electrolyte with higher ionic conductivity (1.4 M LiPF<sub>6</sub> in EC:DEC (3:7 wt) + 2 wt. % VC) is added to the cells. The best results from step (1) and (2) are combined (Figs. 1d, 1e), resulting in the optimized 21700 cells type B-II. In the following sections, each step is discussed in detail in terms of how the different cell parameters influence the charging time to 80% SOC. In order to evaluate the single steps, they are compared to the baseline 21700 cell configuration (1  $\times$  1 welded tabs, electrolyte I, and 1 C CCCV charge).

## Results and Discussion

**Step (1): Charging Protocol.**—The target time to reach a SOC of 80% in this study is 15 min.<sup>2</sup> This means that when using conventional CC charging, a C-rate of 3.2 C has to be applied to reach 80% SOC in 15 min (100% SOC will be theoretically reached in 18 min 45 s). However, higher charging rates lead to higher overvoltages within the cell, e.g. due to transport limitations (see Eq. 1).<sup>3,45</sup>

Figure 2 shows the results of the charge-rate capability test (cells: EL-CR-I). The end-of-discharge capacities are normalized to the discharge capacity of the first cycle. Figure 2a shows that with increasing charging rate, only a fraction of the cell capacity can be utilized. Especially at the high charging rates (2 C, 3 C, and 4 C), capacity retention of about 83%, 77%, and 67% are reached in the EL-CR-I cells. From Fig. 2b, it can be seen that 80% SOC is not reached for the C-rates 2 C, 3 C, and 4 C during CC charging.

Additionally, looking at the anode potentials at these charging rates (Fig. 2b), the anode potential drops below 0 V vs Li/Li<sup>+</sup> already at 2 C. When the anode potential drops below 0 V vs Li/Li<sup>+</sup>, Li metal deposition becomes thermodynamically possible<sup>3,4,19–21</sup> which can cause irreversible capacity losses due to the reaction of Li metal with the electrolyte and electronically insulated Li (“dead Li”).<sup>3,14,46</sup> Especially for high C-rates (2 C, 3 C, and 4 C), the anode potential already drops below 0 V vs Li/Li<sup>+</sup> after a SOC of 53%, 30%, and 18% is reached. The occurrence of capacity losses is evident from the reduced capacity retention in the last 0.1 C cycles (cycle 1–3: SOC: 100%; cycle 19–21; SOC: 97%) and the dropping capacity retention values for the consecutive 4 C cycles in Fig. 2a. From the results shown in Fig. 2, it becomes clear that we cannot reach the target charging time with conventional CCCV charging protocols. The high charging rates needed will lead to fast, irreversible capacity loss due to Li metal deposition on the anode and are a known negative impact on cell stability and aging.<sup>3,21–23</sup>

**Table III. An overview of the advanced MS-CCCV charging procedures used for 21700 type A-I, B-I, and B-II cells.**

Cell Type	1. Step (CC)	2. Step (CV)	3. Step (CC)	4. Step (CV)	5. Step (CC)	6. Step (CV)
A-I	4 C	3.80 V ( $\rightarrow$ 1 C)	1 C	4.0 V ( $\rightarrow$ 0.5 C)	0.5 C	4.2 V ( $\rightarrow$ 0.05 C)
B-I	4 C	3.80 V ( $\rightarrow$ 1 C)	1 C	4.0 V ( $\rightarrow$ 0.5 C)	0.5 C	4.2 V ( $\rightarrow$ 0.05 C)
B-II	4 C	3.85 V ( $\rightarrow$ 1 C)	1 C	4.1 V ( $\rightarrow$ 0.5 C)	0.5 C	4.2 V ( $\rightarrow$ 0.05 C)

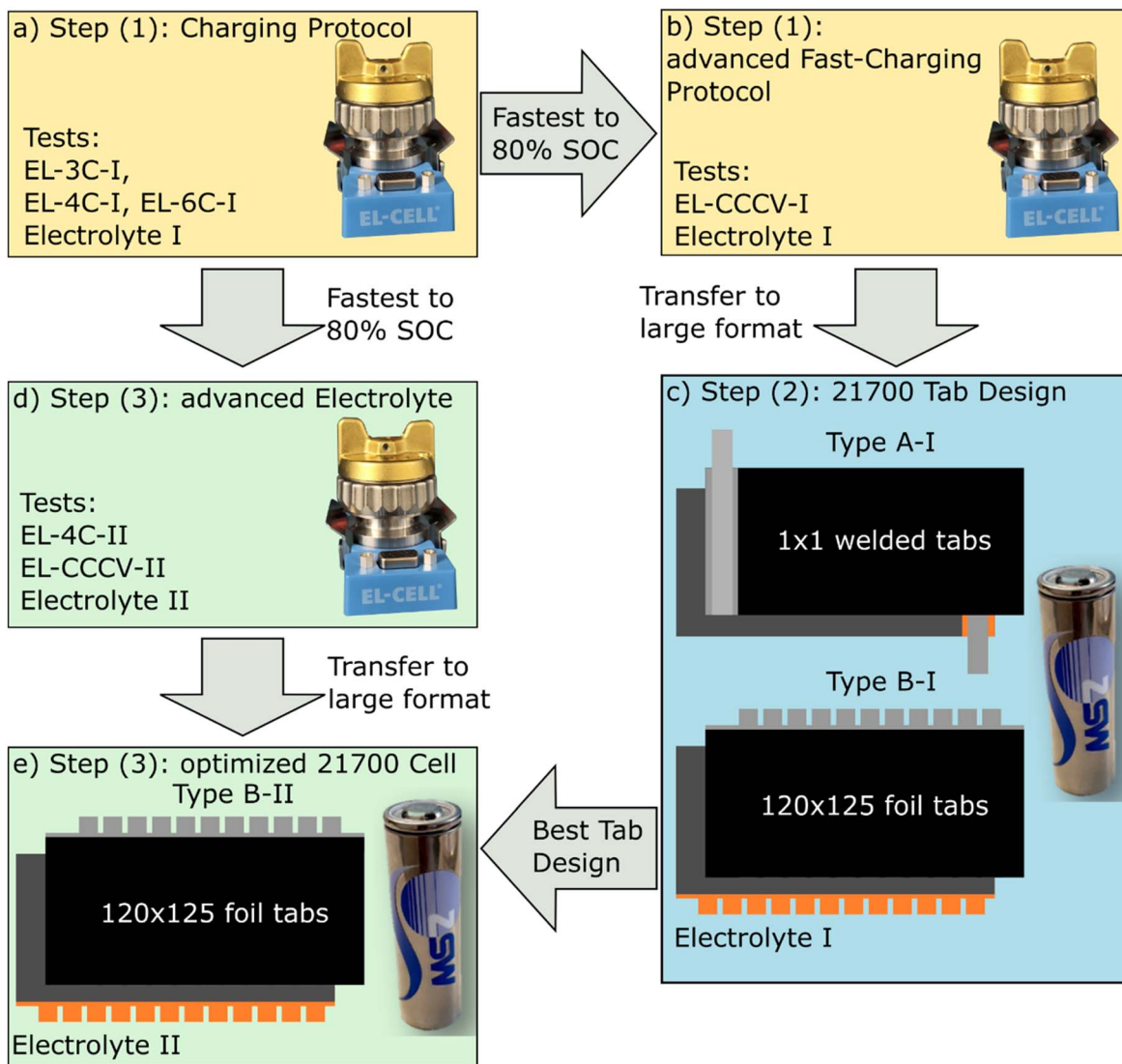


Figure 1. Scheme of the stepwise optimization of the 21700 cell design in terms of the charging time to 80% SOC.

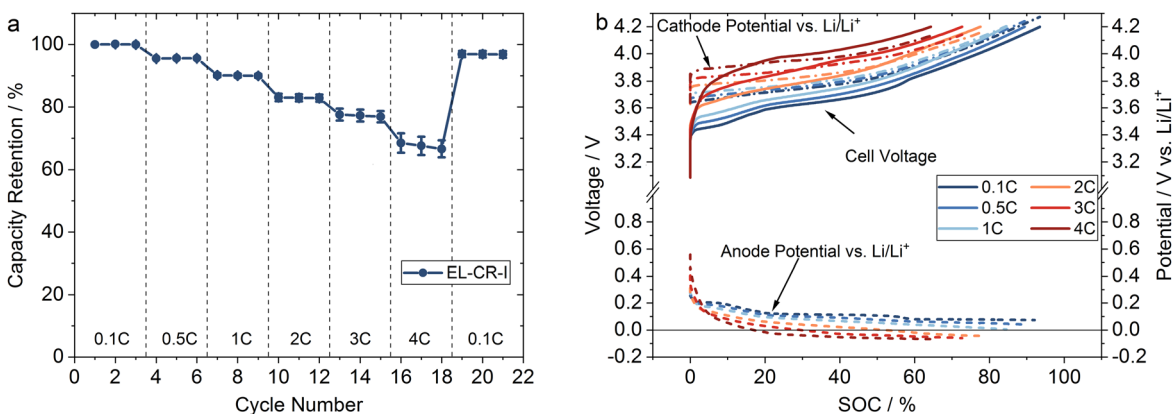
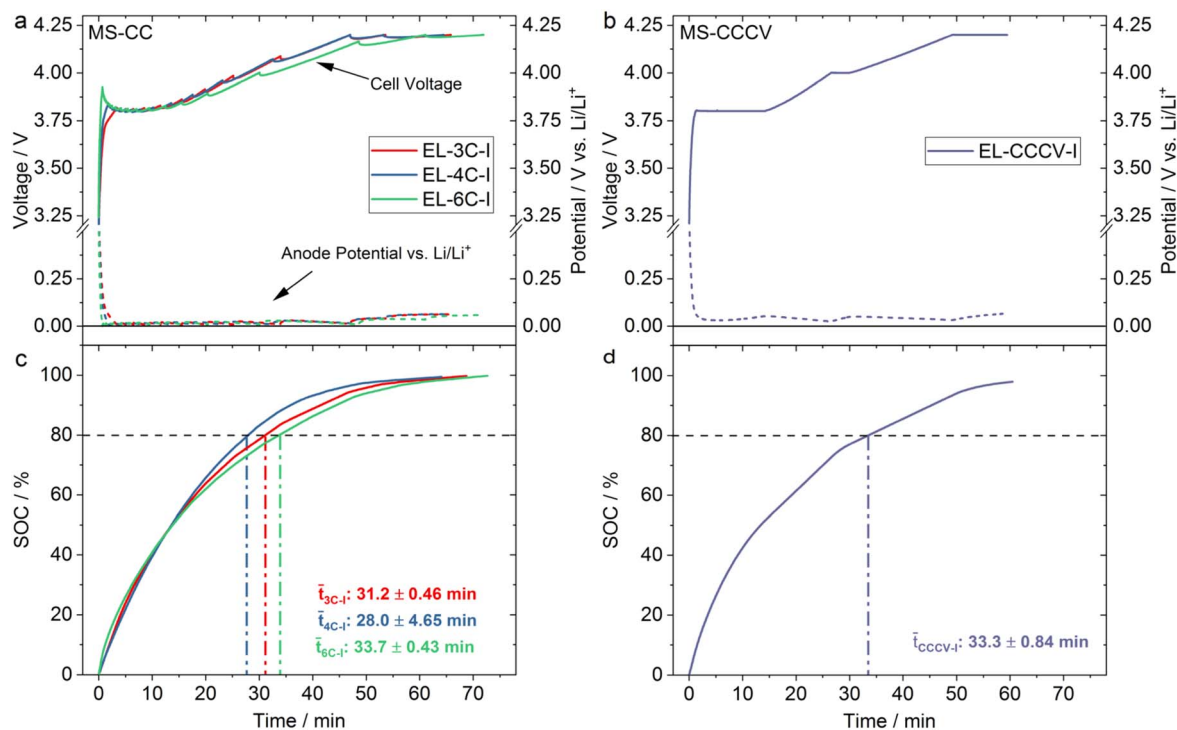


Figure 2. (a) Charge rate-dependent mean capacity retention of the 3-electrode graphite-NMC 622 full cells (EL-CR-I), normalized to the discharge capacity of the first cycle. (b) Cell voltage (solid line), anode potential (dotted line), and cathode potential (dotted-dashed line) for the third cycle of each C-rate from one cell (cycle 3, 6, 9, 12, 15, and 18). The SOC (*x*-axis) is normalized to the discharge capacity of the third formation cycle.

To decrease the charging time and reduce cell aging, sophisticated MS-CC and MS-CCCV protocols must be developed.<sup>24,25,30-34,41,42</sup>

In order to develop a suitable fast-charging protocol for cylindrical 21700 cells, different MS-CC protocols with different starting

C-rates (EL-3C-I: 3 C, EL-4C-I: 4 C, and EL-6C-I: 6 C) were tested (Fig. 3a). The charging rate was reduced by 0.25 C, if the anode potential dropped below +10 mV vs Li/Li<sup>+</sup> or if the cell voltage reached 4.2 V. For all cells, the shape of the voltage profile is similar



**Figure 3.** a) Cell voltage of one exemplary 3-electrode PAT full cell of EL-3C-I, EL-4C-I, and EL-6C-I using a multistage-constant current (MS-CC) charging program with different starting C-rates (3 C—red; 4 C—blue; 6 C—green). The C-rate was reduced by 0.25 C when the cell voltage reached 4.2 V or the anode potential dropped below 10 mV vs Li/Li<sup>+</sup>. b) Cell voltage of exemplary 3-electrode PAT full cells (EL-CCCV-I) charged with the advanced MS-CCCV derived from the 4 C voltage profile in a). c) Time-dependent mean SOC for the different MS-CC charging steps in a). d) Time-dependent mean SOC for the different advanced MS-CCCV charging steps in b). In c) and d), 80% SOC is highlighted by the dotted lines.

as shown in Fig. 3a. This emphasizes the advantage of using reference electrodes in the 3-electrode full cell setup, since it allows tracking of the anode potential. In the first CC-step, the cell voltage rises very quickly. As expected, the steepest cell voltage rise can be observed for EL-6C-I, indicating the highest overvoltages. Consistently, the lowest voltage rise is found for EL-3C-I. After reducing the C-rate, the cell voltage initially drops and rises again within each CC-step. For the first CC-steps, the cell voltage at the end of each step is lower compared to the previous step, leading to local voltage minima. After several of such C-rate steps, the end cell voltage of each step rises again (see Table S1 in the supplementary data). During the entire charging protocol, the anode potential (dotted lines in Fig. 3a) did not drop below 0 V vs Li/Li<sup>+</sup> in all cells. This indicates that Li metal deposition is thermodynamically not possible during charging in the 3-electrode PAT full cells applying the advanced charging protocols.

Figure 3c shows the average time needed to reach the specific SOC for all cells of EL-3C-I, EL-4C-I, and EL-6C-I. The average time to reach 80% SOC was 31.2 min  $\pm$  0.46 min, 28.0 min  $\pm$  4.65 min, and 33.7 min  $\pm$  0.43 min for EL-3C-I, EL-4C-I, and EL-6C-I, respectively. EL-4C-I shows the fastest charging time to 80% SOC but also the largest error. When we consider the standard deviation, the EL-3C-I and EL-4C-I protocols lead to very similar charging times. For the EL-6C-I cells, it seems that reducing the charging C-rates does not cause the overvoltage to decline as much as it does for EL-3C-I and EL-4C-I. Hence, the cell voltage is lower when the charging rate is reduced (compare Table S1 in supplementary data). As the protocol of EL-4C-I is the fastest, this protocol was used as the baseline protocol for the advanced MS-CCCV testing. Looking at Table S1, the end cell voltage is approximately 3.8 V for the C-rates 2 C to 4 C. Therefore, 3.8 V is used as the cut-off voltage for the first CC-step at 4 C. In the first CV-step, the cell is held at 3.8 V until the current drops to 1 C. The second CC-step at 1 C occurs to a cell voltage of 4.0 V. In the second CV-step, the cell voltage is held at 4.0 V, until the current drops to 0.5 C. In the last

CC step, the cell is charged with 0.5 C to the cut-off of 4.2 V and in the last CV step, 4.2 V are held until the current drops to 0.05 C.

The resulting protocol was tested in the cells EL-CCCV-I (Fig. 3b). Using this procedure, the anode potential remains above 0 V vs Li/Li<sup>+</sup>, without controlling the cell via the anode potential. This means that this charging protocol is potentially suitable for 2-electrode full cells without any reference electrode. It is noted that the anode potential rises due to the reduced current in the CV phase in Fig. 3b, which is consistent with our previous results on 3-electrode pouch full cells with a reference electrode and reconstructed electrodes from a commercial 18650 cell.<sup>43</sup> As expected, the charging time to 80% SOC (33.3 min  $\pm$  0.84 min, Fig. 3d) is reduced compared to the pure MS-CC protocols. However, in terms of feasibility, an advanced 3-step MS-CCCV protocol is easier to implement instead of a 16-step MS-CC protocol.

Comparing the charging time to 80% SOC in the PAT EL-Cells of the MS-CCCV (33.3 min) protocol to a 1 C charge (48 min), as it is used in the baseline cell, the charging time is improved by 30%. This shows that the goal of 15 min is not achieved, yet. In order to see the effect of the tab design, the advanced MS-CCCV protocol is tested in 21700 cell types with 1  $\times$  1 welded and 120  $\times$  125 foil tabs in the following section. It was expected that the charging protocols developed in PAT cells could only be a starting point for further optimization when working with 21700 cells. As discussed previously,<sup>5</sup> the cell format has a significant effect on the electrochemical performance, which makes it difficult to directly translate from one cell format to another. For example, there are differences in electrode areas. Therefore, we expect a larger contribution to  $\eta_{ohm}$  in the PAT-cells due to the smaller electrode area (2.54 cm<sup>2</sup>).<sup>4,5</sup> Even within one cell type, the cell design can highly influence the electrochemical performance.<sup>5,26,27</sup> In cylindrical cells, changes in the tab design can increase the cycle life of the cell, by for example, reducing the cell resistance.<sup>27</sup> Additionally, one layer of GF/A (260  $\mu$ m) was used within the PAT-cells instead of Celgard (25  $\mu$ m). GF/A was chosen to ensure good wetting of the Li reference ring.

However, the larger distance between anode and cathode most likely contributed to the overvoltage of the cell due to the  $IR$ -drop in the electrolyte.<sup>4,47</sup>

Another difference between the 21700 and the PAT-cells is the overhang area. As discussed previously,<sup>13,48</sup> changing the areal ratio between anode to cathode results in different capacities. In order to avoid issues due to the electrode alignment, the same electrode area for both anode and cathode was chosen in the PAT-cells. In contrast, the usual anode overhang (length: 2.5 cm in both directions, width: 1 mm in both directions) was used in the 21700 cells. Since introducing a reference electrode in between the electrodes disturbs cycling conditions within the cell,<sup>49</sup> and positioning of the reference electrode is critical for reliable results,<sup>50</sup> we decided conducting pre-tests in PAT-cells. It should be noted that the placement of the ring reference at the edge of the stack probably causes some additional overpotentials due to the  $IR$ -drop in the electrolyte.<sup>51</sup> However, Sieg et al.<sup>32</sup> used a similar approach to conduct pre-tests in PAT-cells in order to generate data for their algorithm before testing different current profiles in large format cells. Due to the previously mentioned reasons, we expect faster charging in the 21700 cells compared to the PAT-EL cells.

**Step (2): 21700 tab design.**—Figure 4 shows the differences between the 1 C CCCV charge and advanced MS-CCCV charge in the cylindrical cell types A-I ( $1 \times 1$  welded tabs) and type B-I ( $120 \times 125$  foil tabs). When comparing type A-I with type B-I, it can be seen that type B-I exhibits lower overvoltages than type A-I during a 1 C CCCV charge (Fig. 4a). In the advanced MS-CCCV protocols, the higher overvoltages are noticeable by the inability to charge the type A-I cells with 4 C at the beginning of the charging procedure (Figs. 4a, 4b). The cells immediately reach the first cut-off voltage of 3.8 V, starting charging in the CV step. Therefore, the type B-I cells can be charged with a higher average current for a longer time compared to type A-I (Fig. 4b).

The effects on charging time in terms of capacity can be seen in Fig. 4c. During the 1 C CCCV charge, both type A-I and B-I reach 80% SOC after 45 min. Type A-I reaches 80% SOC after  $42.75 \text{ min} \pm 2.12 \text{ min}$  during the advanced MS-CCCV charge, being only 3 min faster than the 1 C CCCV charge. Considering the standard deviation between the cells, this difference is insignificant. However, type B-I shows a significant reduction of charging time during the advanced MS-CCCV charge: 80% SOC is reached after an average time of  $30.90 \text{ min} \pm 0.61 \text{ min}$ , which is 14 min faster than the corresponding 1 C CCCV charge in the same cells. This means that the tab design ( $120 \times 125$  foil tabs for B-I) and the advanced fast-charging protocol show a synergistic effect.

Figure 4d shows the temperature profile of cell types A-I and B-I during both the 1 C CCCV and the advanced MS-CCCV charge. During the 1 C CCCV charge, the type A-I cells show a similar maximum temperature ( $\sim 28^\circ\text{C} \pm 1^\circ\text{C}$ ) as the type B-I cells ( $\sim 27.5^\circ\text{C} \pm 1^\circ\text{C}$ ). Since the charging rate is still in a moderate range, the effect of cell heating due to Ohmic resistance is expected to be small. It can be noticed that one of the type A-I cells heats up more than the other cell. The temperature profile is very similar but shifted by  $1^\circ\text{C}$  in respect to each other. During the advanced MS-CCCV charge, type B-I cell on average heats up to  $31.7^\circ\text{C}$  within the first 5 min of charging. The type A-I cells show a similar behavior, however the maximum temperature is about  $30.3^\circ\text{C}$ . Again, the shift between the two type A-I cells is noticeable. Considering the error bar of the sensor ( $\pm 1^\circ\text{C}$ ), they heat up in a similar range. After the peak, both type A-I and B-I cells cool down to about  $26^\circ\text{C}$ . As expected, the cooling seems to correspond to the current decline (Fig. 4b).

As seen in Fig. 4, the differences between the cell types become most visible during the advanced MS-CCCV charging. Since type A-I has a higher initial cell impedance at 1 kHz ( $32.55 \text{ m}\Omega \pm 0.55 \text{ m}\Omega$  at 0.25 V) compared to type B-I ( $10.85 \text{ m}\Omega \pm 0.45 \text{ m}\Omega$  at 0.24 V), higher overvoltages due to the higher cell impedance are expected.<sup>4</sup> As discussed in detail by Waldmann et al.,<sup>5,26</sup> the

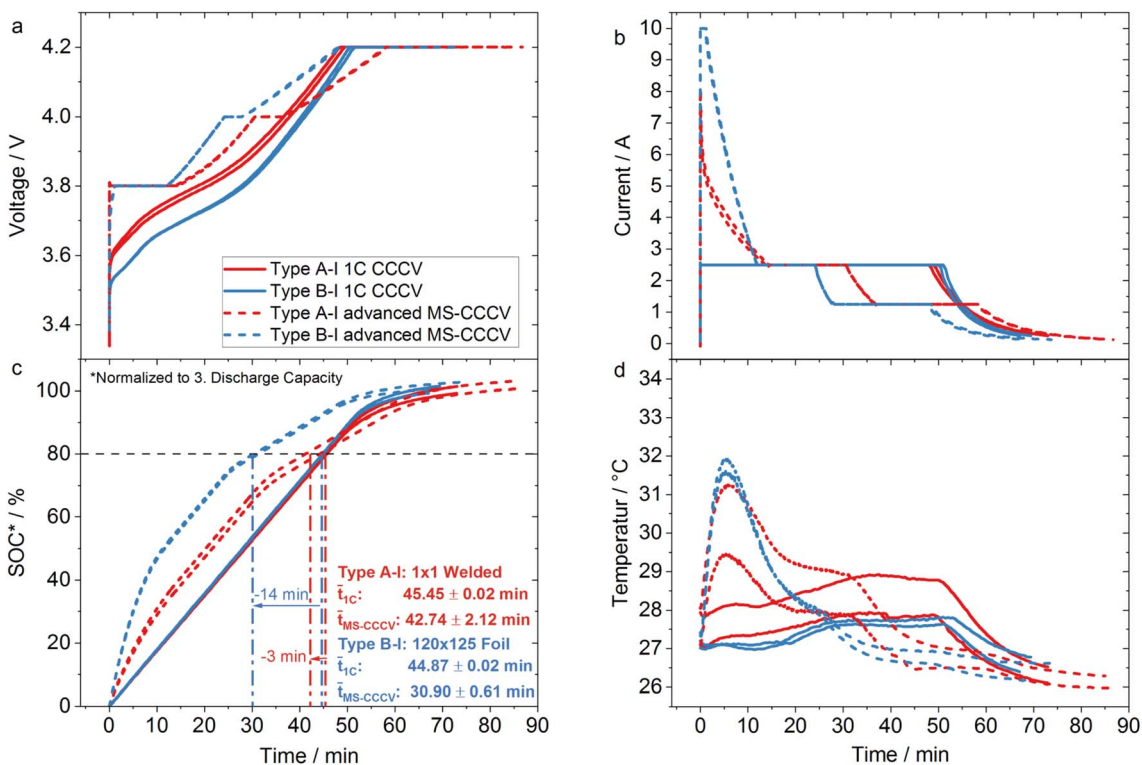


**Figure 4.** Comparison of cell type A-I ( $1 \times 1$  welded tabs—red line) and type B-I ( $120 \times 125$  foil tabs—blue line) during a 1 C CCCV charge (solid line) and advanced MS-CCCV charge (dotted line). a) Cell voltage profiles plotted against the charging time. b) Current during the respective charging procedures. c) Time-dependent SOC curves. The horizontal, dashed line highlights 80% SOC (nominated to 3. discharge capacity of the formation of each cell). d) Temperature profile at mid-height of the cell surface for both cell types for the respective charging profiles.



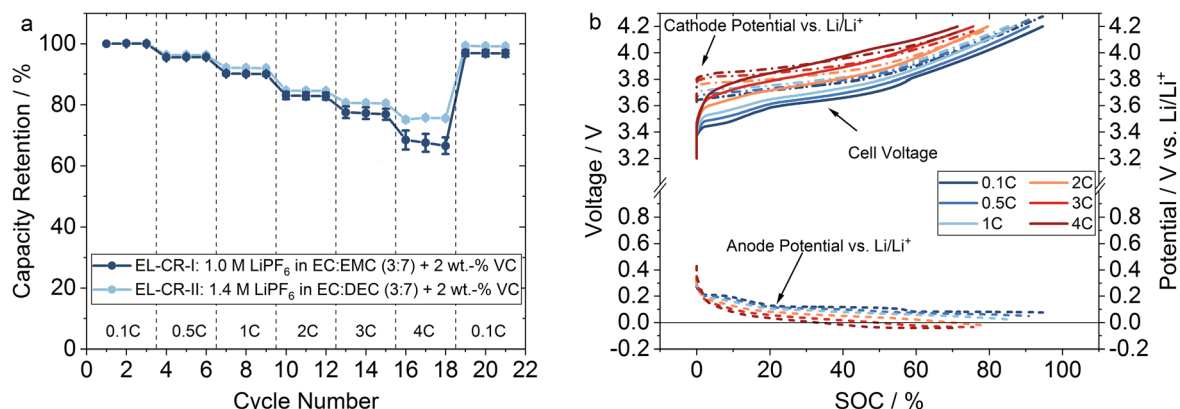


**Figure 5.** a) Charge rate-dependent mean capacity retention of the 3-electrode graphite-NMC 622 full cells (dark blue: EL-CR-I, light blue: EL-CR-II). b) Cell voltage (solid line), anode potential (dotted line), and cathode potential (dotted-dashed line) for the third cycle of each C-rate from one EL-CR-II cell (cycle 3, 6, 9, 12, 15, and 18). The SOC (*x*-axis) is normalized to the discharge capacity of the third discharge cycle of the formation.

distance between the anode and cathode tabs strongly influences the cell impedance. The type B-I cells used in this study have a very low minimum distance  $d_{el,min}$  between the opposite tabs of anode and cathode, whereas type A-I cells have a large distance. Sturm et al.<sup>24</sup> showed as well that an increased number of tabs leads to an increased fast-charging capability, since the local polarization is reduced.

When cycling larger format cells, cell heating caused by current flow has to be considered. As can be seen in Fig. 4d for the 1 C CCCV charge, type A-I heats up slightly more than type B-I. This is consistent with the results of others,<sup>24–26</sup> who found a reduced cell heating due to the current flow for cells with a multi-tab design. When looking at the advanced MS-CCCV charge (Fig. 4b), the maximum temperature is very similar although the current is lower for the type A-I cells. If the same current had been applied for the same amount of time, we probably would have observed a higher maximum temperature for the type A-I cells. However, the increased cell temperature can also represent an advantage regarding the avoidance of Li metal deposition. Tippmann et al.<sup>52</sup> found in their simulation that the anode potential shifts to higher values when cell heating due to current flow is considered. Sturm et al.<sup>24</sup> and Frank et al.<sup>25</sup> showed that due to the reduced cell heating in large format cells with an increased number of tabs or tabless design, Li metal deposition becomes more likely in these cells compared to cells with larger cell heating due to the current flow. However, since the cells with the advanced MS-CCCV charging exhibit higher maximum temperatures in the multi-tab cells, we assume that Li metal deposition is still hindered. The possible aging mechanisms are discussed below.

All in all, by combining MS-CCCV charging from step (1) with a cell design with low cell impedance ( $120 \times 125$  foil tabs), the charging time to 80% SOC can be reduced to 30 min. Compared to the baseline 21700 cell ( $1 \times 1$  welded tabs, 1 C CCCV charge), this corresponds to an improvement of 33%. However, the target time of 15 min is still not reached. Therefore, the next step is to change the electrolyte in the 21700 type B cells to one with increased ionic conductivity in order to improve the  $\text{Li}^+$  transport within the cell.

**Step (3): Electrolyte.**—A fast mass transport through the electrolyte and within the electrode is crucial for enabling good fast-charging capabilities.<sup>3,9</sup> There are different approaches to achieve improved mass-transport: On the one hand, the electrode microstructure can be modified to reduce ionic pathways.<sup>7,11,12,53–58</sup> On the other hand, electrolytes with higher ionic conductivity can be used.<sup>16,17</sup> In this study, we chose an electrolyte with increased ionic conductivity (electrolyte II: 1.4 M  $\text{LiPF}_6$  in EC:DEC (3:7 wt) + 2 wt. % VC: 12  $\text{mS cm}^{-1}$  at 25 °C). The ionic conductivity is 33% higher compared to the ionic conductivity of the initial electrolyte I (1.0 M  $\text{LiPF}_6$  in EC:EMC (3:7 wt) + 2 wt. % VC: 9  $\text{mS cm}^{-1}$  at 25 °C).

The better fast-charging performance of cells using electrolyte II is also visible in the charging rate capability tests of the EL-CR-II (Fig. 5). The capacity retention values for EL-CR-II in Fig. 5a are slightly higher than for EL-CR-I, especially at higher charging rates (2 C, 3 C, and 4 C). Although the anode potential still drops below 0 V vs  $\text{Li/Li}^+$  at these C-rates (Fig. 5b), the intersection with the 0 V vs  $\text{Li/Li}^+$  line is at higher SOC values for EL-CR-II compared to the EL-CR-I cells (Fig. 2b). For 2 C, 3 C and 4 C in Fig. 5b, the anode potential drops below 0 V vs  $\text{Li/Li}^+$  in the EL-CR-II cells at a SOC of 70%, 50%, and 33%, respectively (EL-CR-I in Fig. 2b: SOC: 53%, 30%, 18% for 2 C, 3 C, and 4 C, respectively). Therefore, we expect less Li metal deposition in the EL-CR-II cells. When looking at the second 0.1 C cycles, EL-CR-II still reaches >99% capacity retention after the rate capability test. EL-CR-I exhibits losses and only reaches 97% capacity retention in the second 0.1 C cycles.

Based on the better rate capability, we expect further improvement in the charging time to 80% SOC. Therefore, pre-tests were performed in 3-electrode PAT full cells to determine a suitable advanced MS-CCCV charging protocol (Fig. 6) before testing the electrolyte in 21700 cells. The starting C-rate was chosen to be 4 C to ensure the same starting current density in the cylindrical cells. The MS-CC charging protocols, which are led by the anode potential, for both 3-electrode PAT cells with electrolyte I (EL-4C-I) and electrolyte II (EL-4C-II) are shown in Fig. 6a. It can be observed that the EL-4C-II cells reach the cut-off criteria (anode potential <10 mV vs  $\text{Li/Li}^+$  or cell voltage >4.2 V) later and at higher cell voltages (see Table S1 in supplementary data) than the EL-4C-I cells. When looking at Fig. 6c, it can be clearly seen that the SOC is rising much steeply for the EL-4C-II cells than the EL-4C-I cells. A SOC of 80% was reached in 22.2 min  $\pm$  1.91 min in the EL-4C-II cells, which is 21% faster than the EL-4C-I cells. Fig. 6b shows the resulting advanced MS-CCCV charging protocols of EL-4C-I and EL-4C-II. Since the cut-off criteria were reached after a longer charging time and at higher cell voltages in the EL-4C-II cells, the cut-off voltages in the EL-CCCV-II cells are higher (compare Table III, cell type B-II). Besides the voltage cut-off, the C-rates were kept the same. Again, the resulting advanced MS-CCCV protocol is slower than the MS-CC protocols. Still, 80% SOC are reached after 25.5 min  $\pm$  0.27 min in the EL-CCCV-II cells with this advanced MS-CCCV protocol, which is 23% faster than the EL-CCCV-I cells (Fig. 6d) and 47% faster compared to the 1 C charge (48 min) of the baseline cell configuration.

In order to get an idea of the effect of the higher ionic conductivity in 21700 cells, cell type B-I and B-II are directly compared in Fig. 7. Since the initial cell impedance  $Z$  at 1 kHz difference is small (type B-I: 10.85  $\text{m}\Omega \pm$  0.45  $\text{m}\Omega$  at 0.24 V; type B-II: 9.45  $\text{m}\Omega \pm$  0.13  $\text{m}\Omega$  at 0.21 V), the differences during the 1 C CCCV charge are small as well (Fig. 7a).

It has to be noted that it seems like 80% SOC is reached 3 min later in type B-II than in type B-I in Fig. 7c. However, the SOC is

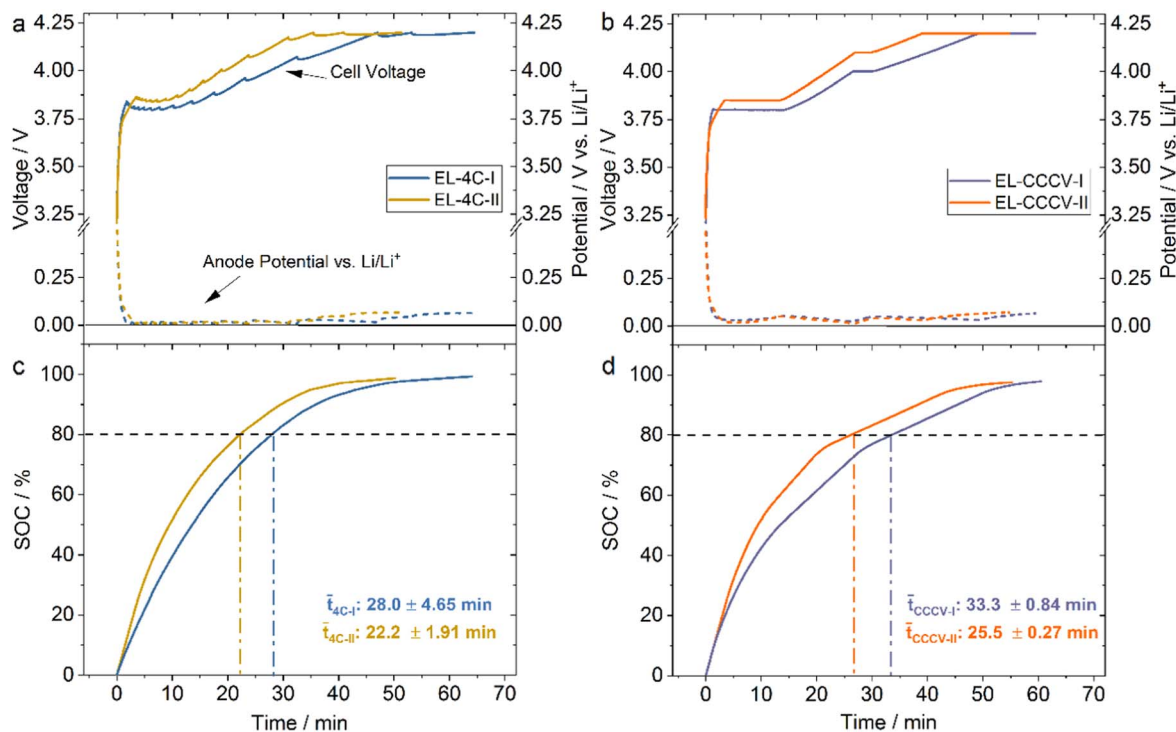


**Figure 6.** a) Cell voltage of exemplary PAT full cells EL-4C-I and EL-4C-II with different electrolytes using a MS-CC charging program (electrolyte I: 1.0 M  $\text{LiPF}_6$  in EC:EMC (3:7 wt) + 2 wt. % VC—blue; electrolyte II: 1.4 M  $\text{LiPF}_6$  in EC:DEC (3:7 wt) + 2 wt. % VC—yellow). The C-rate was reduced by 0.25 C when the cell voltage reached 4.2 V or the anode potential dropped below 10 mV vs  $\text{Li/Li}^+$ . b) Cell voltage of full cells (EL-CCC-V-I - purple and EL-CCC-V-II—orange) charged with the advanced MS-CCC-V derived from the voltage profile in a). c) Time-dependent mean SOC for the different MS-CC charging steps in a). d) Time-dependent mean SOC for the different advanced MS-CCC-V charging steps in b). In c) and d), the SOC is normalized to the third discharge capacity of the formation cycle. 80% SOC is marked by the dashed vertical lines.

calculated by normalizing towards the discharge capacity of the third formation cycle. In the type B-II cells, this capacity was higher ( $2.22 \text{ Ah cm}^{-2}$ ) than in the type B-I cells ( $2.11 \text{ Ah cm}^{-2}$ ). Since the cells were manufactured in different batches in our facility, small differences cannot be ruled out. We did not observe a similar effect in the other cell formats.

The differences in the advanced MS-CCC-V charge are more noticeable. Since higher cut-off voltages in the individual charging steps are possible with the MS-CCC-V protocol (see Fig. 6a and Table III) the 4 C charge in the beginning lasts for several minutes (3.85 min, 1.22 min for type B-I) in the type B-II cells (Fig. 7a). This corresponds to higher charging currents at the beginning of charging (Fig. 7b) and therefore 80% SOC is already reached after  $25.04 \pm 0.51$  min, being 22 min faster than the standard 1 C CCCV charge in the same cells. Compared to the type B-I advanced MS-CCC-V protocol, the protocol used in the type B-II is 5 min faster. However, the faster charging also affects the heating of the cell due to the higher current flow (Fig. 7d). The temperature on the surface rises up to a maximum of about  $33.6^\circ\text{C}$  within the first 7 min. The type B-I cells reach the maximum temperature after 5 min ( $31.7^\circ\text{C}$ ), which is only slightly lower. With decreasing current (Fig. 7b), the temperature of both type B-I and B-II decreases to the initial value of about  $26^\circ\text{C}$ .

Overall, the combination of charging protocol, 21700 tab design, and improved electrolyte lead to a 46% improvement in charging time to 80% SOC compared to the baseline cell. However, the goal of 15 min was not achieved. In the next section, the effect of the improved ionic transport in terms of graphite lithiation is discussed by cross-sectional in situ optical microscopy. Afterwards, the effect of the optimization on the aging behavior of the 21700 cells is discussed.

**Visualization of improved ionic transport.**—In order to visualize the differences in ionic transport properties of different electrolyte

solutions, we conducted measurements using cross-sectional in situ optical microscopy. Different in situ cells with both electrolyte I and II were charged at 0.75 C (calculated based on the theoretical capacity of the cathode) after having completing one initial formation cycle at 0.1 C CCCV.

The effect of the better ionic transport properties on the lithiation of the anode is visible, both in the coloring of the anode and the end-of-charge (EoC) SOC's of electrolyte I in Fig. 8. Figure 8a shows the images for one in situ cell using electrolyte I and II at the SOC (referenced to discharge capacity of the first cycle) values of 0%, 10%, 20%, 30%, 40%, 50%, 60%, 70%, 80%, 90%, and 100%. The electrolyte I in situ cell includes an EoC image at 105% SOC, since the cell exceeded the capacity discharged in the previous cycle. For the electrolyte I cell in Fig. 8a, the anode is mostly colored golden ( $\text{LiC}_6$ )<sup>59,60</sup> at 40% SOC, whereas the electrolyte II cell is completely red ( $\text{LiC}_{12}$ ).<sup>59,61</sup> A similar trend was observed for the reproduced in situ cells for both electrolytes, shown in Fig. S1 in the supplementary data. All measured in situ cells using electrolyte I exhibited SOC values larger than 100% at EoC. Although no Li dendrites are observable in the investigated part of the cross-section, the overcharge of the cells indicates internal short circuits.<sup>14</sup> Additionally, it can be observed for the in situ cells using electrolyte I that the current does not drop regularly during the CV-step, but exhibits noisy features (Figs. 8b, S1b). We assume that these internal short circuits have been caused by Li dendrites, as observed in our previous publication.<sup>14</sup> On the contrary, the cells with electrolyte II do not exceed 100% SOC after the EoC, indicating no or no significant amount of Li metal deposition, and beneficial charging performance.

It is evident from Fig. 8b, where we see a larger variation in the cell voltage of the two in situ cells at 0.75 C, as we would have expected from the differences observed in the 21700 cells at 1 C for the cell type B-I and B-II (Fig. 7). As previously discussed in step (1) and in a publication from our group,<sup>5</sup> different cell formats can

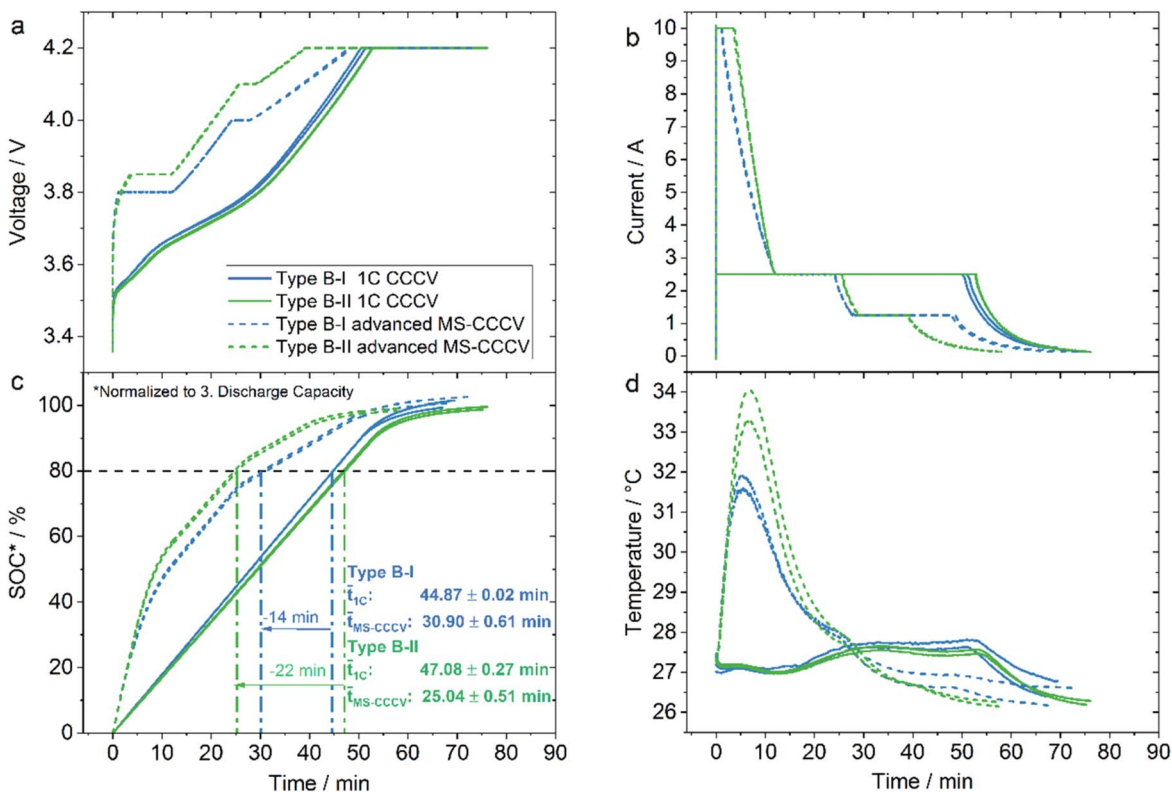


**Figure 7.** Comparison of 21700 cell type B-I ( $120 \times 125$  foil tabs,  $1.0 \text{ M LiPF}_6$  in EC:EMC (3:7 wt) + 2 wt% VC—blue line) and type B-II ( $120 \times 125$  foil tabs,  $1.4 \text{ M LiPF}_6$  in EC:DEC (3:7 wt) + 2 wt% VC—green line) during a 1 C CCCV charge (solid line) and advanced MS-CCCV charge (dotted line). a) Cell voltage profiles plotted against the charging time. b) Current during the respective charging procedures. c) Time-dependent SOC curves. The horizontal, dashed line emphasizes 80% SOC. d) Temperature at mid-height of the cell surface for both cell types for the respective charging profiles.

have a huge effect on cell voltage. Additionally, we have to consider the edge effect in the in situ optical cell (no anode and separator overhang due to cross-sectioned cell), which causes higher local current densities at the observed area in the in situ cells,<sup>14,62</sup> as well as a slightly different formation procedure. However, the in situ optical microscope is a tool for visualization of the lithiation behavior of graphite anodes, which is how it was used in this study. Overall, Fig. 8 substantiates the results from optimization step (3), visualizing the beneficial effect of the better ionic transport on the fast-charging capability, which leads to the increased performance of the optimized 21700 cell type B-II.

**Aging.**—Fast-charging is known to decrease the cycle life of battery cells, since high C-rates induce cycle-life reducing side-reactions such as Li metal deposition on the anode side.<sup>18</sup> Therefore, the different 21700 cell configurations were aged. The results of the cycling aging are shown in Fig. 9. The state-of-health (SOH) is normalized to the discharge capacity of the first aging cycle. The check-up cycles at 0.2 C are not shown in Fig. 9. During cycling, an increase of SOH is observed at around 200 and 400 cycles, respectively. This increase of SOH results from internal cell heating due to a defect of the climate chamber. However, we believe that it has little effect on the overall aging behavior, as the SOH values fit to the linear behavior of the  $25^\circ\text{C}$  aging after the temperature was controlled again. It is noticeable that the aging is more stable during the first 500 cycles for the type A-I cells ( $1 \times 1$  welded tabs) than for type B-I and B-II ( $120 \times 125$  foil tabs). After a linear decrease and regardless of the electrolyte used all type B cells exhibit a drastic capacity decline after  $\sim 350$  cycles. Therefore, one type B-I cell was opened after aging at a SOH of 82%. Due to the drastic capacity decay at the end of cycling, we expected a larger amount of Li metal deposition on the anode surface. However, only small amounts of white deposits (presumably Li metal) were found on the anode surface. However, delamination of the anode coating on the casing

side was seen after cell disassembly (compare Fig. S2). The exact source of the drastic capacity fade in the type B cells is still under investigation in our laboratories.

The aging rate was analyzed by linear regression using the linear parts in Fig. 9. Since the type B cells exhibit drastic capacity fade, only the first 350 cycles were considered for the linear regression. Up to 350 cycles, all cells show  $R^2$  values  $\geq 0.986$ , showing the very good agreement with the least-square linear fit calculation. The resulting aging rates are shown in Table IV. For the type A-I cells, the advanced MS-CCCV cells seem to age 11% slower during the first 350 cycles than the cells aged with 1 C CCCV. However, when looking at the cell voltages during aging, it can be seen that the type A-I advanced MS-CCCV cells sometimes skipped the first CCCV step at high current-rates (see Fig. S4 in supplementary data). We assume this happened due to the high overvoltages. In these cycles, the cells were charged more slowly than the type A-I cells with the 1 C CCCV aging. Therefore, it is difficult to attribute the reduced aging rate to the advanced MS-CCCV (fast-)charging.

Before the sudden capacity drop, the type B-I with 1 C CCCV cells age similarly to the type A-I advanced MS-CCCV cells. However, we can see that the aging is quite accelerated by the advanced MS-CCCV charging: Type B-II advanced MS-CCCV aged 40% faster than type B-I 1 C, type B-II aged even 47% faster. One contribution to the faster aging could be the stronger heating of the cells due to the higher current flow. Table IV shows the mean maximum temperature on the casing during the first 350 cycles (compare Fig. S3). We note that the temperature sensors of one type A-I cells aging disconnected during 1 C CCCV test after cycle 36 (\* in Table IV). Therefore, the mean maximum temperature in Table IV does only refer to these cycles for this cell. For all other cells, the same cycles as for the aging rate are considered. The cells with the highest aging rate (type B-II) also exhibits the highest maximum temperature. It is known that cycling at higher temperatures leads to accelerated aging due to increased side-reactions, such as SEI

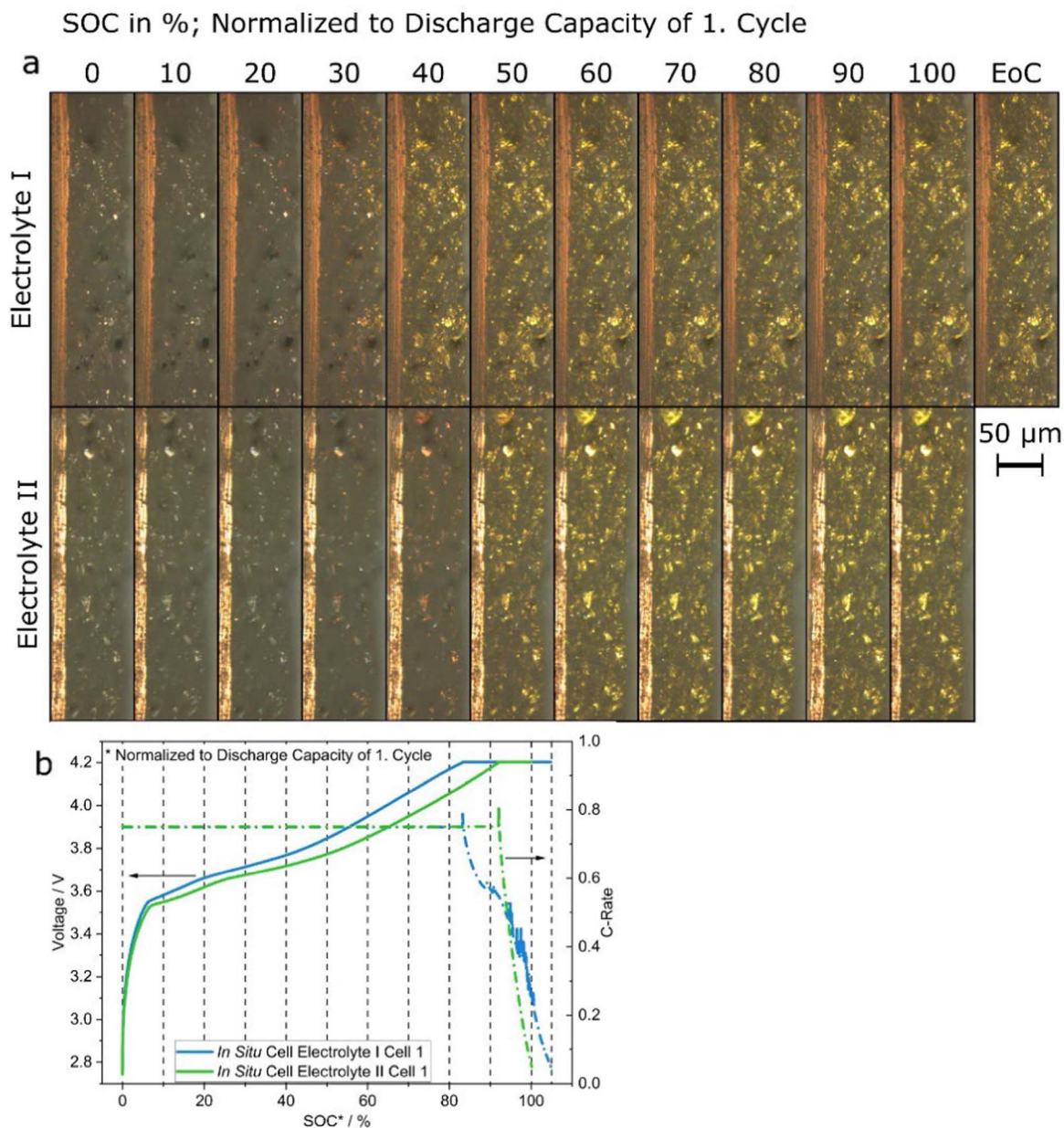


**Figure 8.** (a) Images of the anodes of in situ cells using electrolyte I (upper panel, cell 1) and electrolyte II (lower panel, cell 1) during different SOC during a 0.75 C charge. The observed colors correspond to the lithiated graphite phases  $\text{LiC}_{18}$  (blue),  $\text{LiC}_{12}$  (red), and  $\text{LiC}_6$  (yellow/gold).<sup>59–61</sup> The videos of the corresponding measurements can be found as video S1 (electrolyte I) and video S2 (electrolyte II) in the supplementary data. For electrolyte I, an additional image of the anode at the end-of-charge (EoC) is shown. (b) Cell voltages (solid line) and C-rates (dotted line) of the in situ cells in (a). The vertical dashed lines highlight the SOC values from the images in (a). The blue line corresponds to the in situ cell with electrolyte I and green line to the in situ cell with electrolyte II.

growth.<sup>21</sup> On the other hand, higher temperatures and larger heating of cells were found to reduce the likelihood of Li metal deposition on the anode.<sup>24,25</sup> This is consistent with the observations from the cell disassembly for one cell of the type B-I cell after aging, where only small amounts of presumably Li metal deposits were found. Looking at the change in cell resistance measured by DCIR (Table IV, Fig. S4), it can be seen that the absolute change for all cells is in a very similar range ( $\Delta \text{DCIR} = 17\text{--}22 \Omega \text{ cm}^2$ ). Additionally, it seems like that the drastic capacity fade does not influence the cell resistance measured by DCIR. Therefore, we assume that all cells age with the same aging mechanism during the linear part, presumably SEI growth. Since we did not perform further Post-Mortem analysis, we cannot be sure about the final aging mechanisms. Since we see the drastic capacity decline in the type B cells, we assume a second aging mechanism happens, which does not affect the cell resistance measured by DCIR.

Summarizing, the MS-CCCV charging protocols were designed to avoid the thermodynamic conditions for Li metal deposition (anode potential  $< 0 \text{ V vs Li/Li}^+$ ). This goal was achieved since no evidence of significant amounts of Li metal deposition upon disassembly of one cell at 80% SOH. However, accelerated aging was found for the optimized 21700 cells compared to the baseline cell with 1 C CCCV charging. Possibly, the increased cell heating due to the current flow during the advanced MS-CCCV charging protocols enhances the SEI growth, which leads to loss of active Li within the cells.

**Evaluation of combination of single optimizing processes.—** Figure 10 shows an overview of the stepwise optimization from the initial  $1 \times 1$  welded tab design to the  $120 \times 125$  foil tab design for 21700 cells using an advanced MS-CCCV charging protocol and an electrolyte with increased ionic conductivity. By only changing the

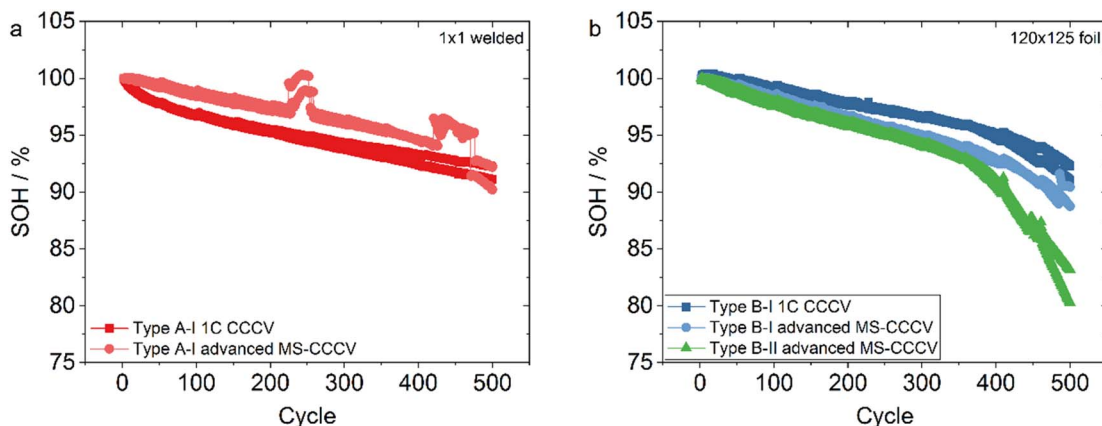


**Figure 9.** State-of-Health (SOH) of the (a) type A-I (red), (b) type B-I (blue) and type B-II (green, triangle) cells during aging with 1 C (squares) and advanced MS-CCCV (circles) plotted against cycle. The SOH is normalized to the discharge capacity of the first aging cycle. The check-up cycles at 0.2 C are not shown in the aging plots.

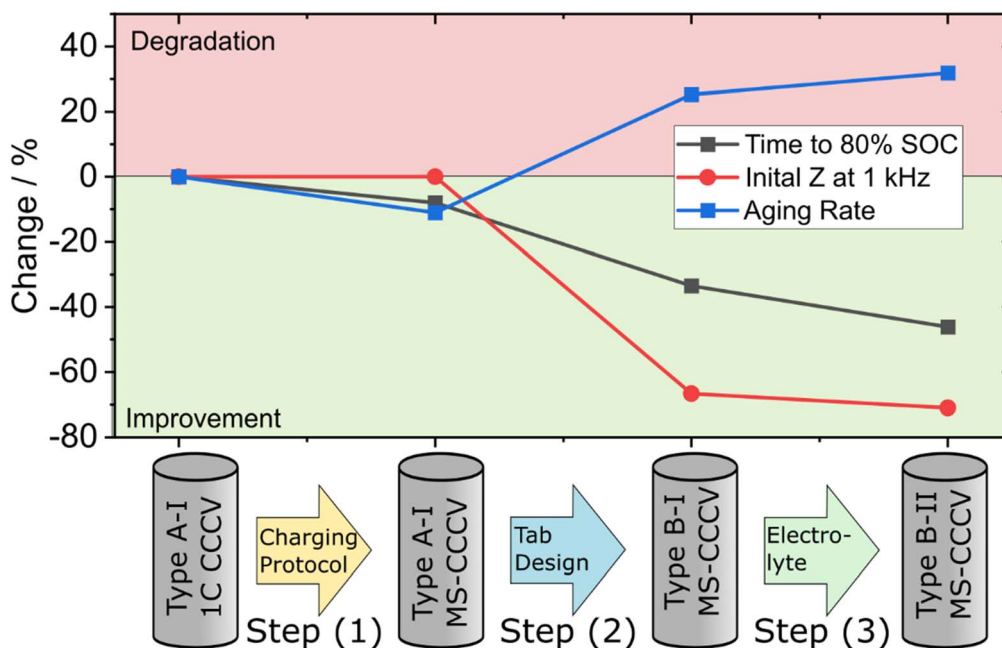


**Figure 10.** Summary of the stepwise cell design changes within this study and the corresponding changes in charging time to 80% SOC (black square), the initial cell impedance Z at 1 kHz (red dots), and the aging rate (blue squares). The type A-I 1 C CCCV charging is used as the baseline. Positive values indicate degradation from the baseline. Negative values indicate an improvement from the baseline.

**Table IV.** Aging rates, maximum temperature and changes in DCIR for the different cylindrical cell types for the different aging procedures. The aging rate was determined in the linear parts of the first 350 cycles by linear regression of the curves in Fig. 9a.

Cell type	Charging protocol	Analyzed cycles	Aging Rate/% Cycle <sup>-1</sup>	R <sup>2</sup>	Max. temperature /°C	Δ DCIR/Ω cm <sup>2</sup> (cycle 1–409)
A-I	1 C	30–350	$-0.01559 \pm 7.2 \cdot 10^{-5}$	0.994	$27.9 \pm 0.03$ (1–36)*	17.2
A-I	1 C	30–350	$-0.01331 \pm 8.9 \cdot 10^{-5}$	0.986	$26.9 \pm 0.16$	17.0
A-I	advanced MS-CCCV	1–350	$-0.01299 \pm 5.2 \cdot 10^{-5}$	0.994	$31.3 \pm 1.15$	19.4
A-I	advanced MS-CCCV	1–350	$-0.0127 \pm 4.0 \cdot 10^{-5}$	0.997	$29.4 \pm 0.92$	19.0
B-I	1 C	1–350	$-0.01304 \pm 5.5 \cdot 10^{-5}$ ;	0.994	$27.7 \pm 0.30$	19.0
B-I	1 C	1–350	$-0.01283 \pm 3.8 \cdot 10^{-5}$	0.997	$27.7 \pm 0.64$	19.3
B-I	advanced MS-CCCV	1–350	$-0.01871 \pm 3.4 \cdot 10^{-5}$	0.999	$33.4 \pm 3.28$	22.1
B-I	advanced MS-CCCV	1–350	$-0.01749 \pm 3.4 \cdot 10^{-5}$	0.999	$31.0 \pm 0.49$	21.0
B-II	advanced MS-CCCV	1–350	$-0.01961 \pm 5.5 \cdot 10^{-5}$	0.998	$33.5 \pm 0.09$	18.8
B-II	advanced MS-CCCV	1–350	$-0.01849 \pm 7.4 \cdot 10^{-5}$	0.995	$34.1 \pm 0.07$	19.2

charging protocol, the charging time to 80% SOC is improved by 8%. The aging rate decreases by 11% as the average C-rate was lower in several cycles compared to the baseline cell (compare Fig. S4). Additionally, by changing the tab design from  $1 \times 1$  welded tabs to  $120 \times 125$  foil tabs, the initial cell impedance  $Z$  at 1 kHz of the cell is reduced by 67%. The charging time to 80% SOC is reduced to 30.9 min, which corresponds to an improvement of 33% compared to the baseline cell. If an electrolyte with better ionic transport properties is used, the charging time to 80% SOC is further decreased to 46% of the initial value. In our experiments, the improvement in fast-charging capability came at the cost of accelerated cell aging. The aging rate for type B-I and type B-II using an advanced MS-CCCV protocol increases by 37% and 39%, respectively, compared to the baseline cell configuration (Type A-I, 1 C CCCV).

Overall, we did not achieve the charging time goal of 80% SOC in 15 min. However, we were able to improve the charging time to 80% SOC in your final cell by 46% compared to our baseline cell configuration without changing the electrodes. This corresponds to a charging time of 25 min at 25 °C using the advanced MS-CCCV charging protocol, the  $120 \times 125$  foil tab design, and a more suitable electrolyte. On cell level, the largest contribution to the overall 46% improvement was the reduction of cell impedance  $Z$  at 1 kHz of the cylindrical cell. Using the same advanced MS-CCCV charging protocol, the resulting charging times to 80% SOC varied significantly. The effect of the advanced MS-CCCV protocol is highly dependent on the ionic transport properties, as demonstrated in the pre-tests with both electrolyte solutions. The next steps would be, to further improve the kinetics within the cells further by improving the electrodes in terms of better fast-charging capability. Therefore, many approaches have been published at the electrode and material level:

On the anode side, spheroidization of the graphite particles enables faster intercalation kinetics.<sup>63,64</sup> Another way to improve the fast-charging capability is to mechanical structure high energy electrodes to improve ionic pathways through the electrode, e.g. by laser structuring.<sup>53,55–58</sup> Billaud et al.<sup>65</sup> magnetically aligned graphite flakes, which have previously treated with superparamagnetic iron oxide nanoparticles, in thick, high loaded electrodes in an out-of-plane architecture, which highly reduced the electrode tortuosity and increased the charging rate performance.<sup>65</sup> Edging of graphite active material with KOH introduces nano-sized pores on the graphite surface that serve as additional intercalation sites into the graphite layers.<sup>66,67</sup>

Comparing our 80% charging time with others reported in literature using similar temperatures, MS-CCCV charging protocols and cell formats, it is noticeable that we are in the same range, demonstrating the limitations of the pure multistage approach: Frank et al.<sup>25</sup> reported MS-CCCV charging procedures, which charge 18650 cells to 80% SOC in 22 min in without Li metal deposition, using a multidimensional, multi-physics modeling framework that tested different cooling topologies and cell tab designs. Hu et al.<sup>41</sup> determined a MS-CC<sup>3</sup> charging protocol for 18650 cells using a coupled model for the investigated including a electrochemical model, single-state thermal model and an empirical capacity-fade model, where the cells are charged from 10% SOC to 90% SOC ( $\Delta 80\%$ ) in 28 min. Their balanced charging protocol, which is a trade-off between charging time, aging, and battery temperature, requires 50 min to achieve  $\Delta 80\%$  SOC.<sup>41</sup> Sieg et al.<sup>32</sup> reported a charging time of 39 min to 80% SOC in pouch cells using a MS-CC<sup>5</sup>-CV protocol at 25 °C. They managed to further reduce the charging time by using current profiles instead of multiple current stages. Their determined current map protocols needed about 15 min to reach 80% SOC at both pouch cell and battery pack level.<sup>32</sup> As seen in the mentioned examples, the combination of modeling, real-time computation, and simulation can be used to predict limiting parameters such as Li metal deposition conditions, critical temperatures and currents, and reduce the number of experiments needed to determine optimal charging

protocols.<sup>25,30,36,41,68</sup> The model-based computation approach could be used to overcome the gap between the critical anode potential of 0 V vs Li/Li<sup>+</sup> and the recorded anode potential of the advanced MS-CCCV charging in Figs. 3 and 6.

Therefore, in order to further reduce charging times on cell level, so-called asymmetric temperature modulation have been tested. By exposing the cell to elevated temperatures (60 °C) for the short period of the charging step, others<sup>34,69</sup> were able to charge LIBs to 80% SOC within 10 min<sup>69</sup> and from 47% to 88% SOC within 5 min<sup>34</sup> using conventional CCCV, respectively. However, rapid heating and cooling battery self-heating structures<sup>70</sup> are needed within the cells in order to achieve homogeneous temperatures within the cells and to keep the exposure to high temperatures as short as possible.<sup>69</sup>

Generally, there many parameters to consider when optimizing a cell regarding fast-charging capability. As the previously discussed results show, without optimized electrodes, the fast-charging target of 15 min to 80% SOC cannot be reached. However, if only the electrodes are considered, the goal cannot be reached either. This study has shown that it is possible to significantly improve the fast-charging performance even without optimized electrodes by changing only some parameters of the 21700 cell.

## Conclusions

In this publication, we optimized the charging protocols of 21700 cells from ZSW pilot manufacturing line towards charging time with the goal to markedly lower charging time to reach 80% SOC. Improvements were made regarding

- (1) the applied MS-CCCV charging protocol avoiding negative anode potentials vs Li/Li<sup>+</sup>,
- (2) 21700 tab design (from  $1 \times 1$  welded tabs to  $120 \times 125$  foil tabs),
- (3) a change of the electrolyte with increased conductivity for Li<sup>+</sup>,

while keeping electrodes and separator unchanged.

Using 1.0 M LiPF<sub>6</sub> in EC:EMC (3:7 wt) + 2 wt% VC as electrolyte, 80% SOC was reached in 28 min in 3-electrode PAT full cells using the anode potential as cut-off criterion (1). This was achieved by starting with a charging rate of 4 C and stepwise reducing the current by 0.25 C. In order to simplify the procedure for cells without a reference electrode, the resulting voltage profile was transferred to an advanced 3-step MS-CCCV profile, resulting in an improvement of 30% in terms of charging time to 80% SOC. This charging profile was tested using 2-electrode 21700 full cells with  $1 \times 1$  welded tabs and  $120 \times 125$  foil tabs (2) manufactured in our pilot line. Using the protocols from (1), 80% SOC was reached in 31 min (+33%), which is 14 min faster than the 1 C charge procedure resulting in similar end-of-charge capacities. Combining the results of (1) and (2) and changing the electrolyte to 1.4 M LiPF<sub>6</sub> in EC:DEC (3:7 wt) + 2 wt% VC, which has a 33% higher ionic conductivity, 80% SOC was reached in 22 min in the 3-electrode full cell pre-tests and in 25.5 min (+46%) in the  $120 \times 125$  foil tab 21700 cells.

Overall, by changing the 21700 cells from the initial conditions ( $1 \times 1$  welded tabs, 1.0 M LiPF<sub>6</sub> in EC:EMC (3:7 wt) + 2 wt. % VC, 1 C CCCV charging) to the optimized parameters ( $120 \times 125$  foil tabs, 1.4 M LiPF<sub>6</sub> in EC:DEC (3:7 wt) + 2 wt. % VC, advanced MS-CCCV charging), the charging time to 80% SOC could be reduced by 46%. However, the faster charging resulted in 39% faster aging by of the 21700 cells, possibly due to increased SEI growth.

To summarize, we have shown that even without optimized electrodes, combinations of single improvements such as fast-charging protocols, cell design, and cell chemistry can lead to significant improvements in the fast-charging capability of Li-ion batteries. These combinations do not necessarily lead to trade-offs, and lead in part to synergetic effects on cell level, resulting in the final optimized cell type B-II. One example of these synergetic

effects shown in this work is the significantly improved fast-charging performance of the  $120 \times 125$  foil tab design compared to the  $1 \times 1$  welded tab design when being charged with the same MS-CCCV charging protocol.

Additional benefits for fast-charging capability can be expected when combining the findings of the present paper with optimized electrodes. Further research in this direction is underway in our laboratories.

### Acknowledgments

ZSW acknowledges funding of the projects RollBatt (03XP0245A) within the ProZell-Cluster and CharLiSiKo (03XP0333A) within the Aqua-Cluster by the German Federal Ministry of Education and Research (BMBF): Project management by Projektträger Jülich (PtJ) is gratefully acknowledged. All investigations in this work were carried out at ZSW's labs. The authors would like to thank the project E-QUAL (03XP0252A) for providing the electrodes (manufactured at ZSW's research production line (FPL)), as well as the ZSW members D. Brändle and F. Falke for building the 21700 cells, R.S. Scurtu for fruitful discussions, A. Aracil Regalado for 21700 cell disassembly, J. Hager for manufacturing of the in situ optical cell, and D. Weirather-Köstner for ionic conductivity measurements.

### ORCID

Thomas Waldmann  <https://orcid.org/0000-0003-3761-1668>

### References

- Bundesministerium für Wirtschaft und Klimaschutz, *Elektromobilität in Deutschland*, <https://bmw.de/Redaktion/DE/Dossier/elektromobilitaet.html> (19.12.2022).
- USABC, *energy-storage-system-goals-ev-goals*, (07.02.2023), <https://uscar.org/download/246/energy-storage-system-goals/12840/low-cost-fast-charge-ev-goals.pdf>.
- M. Weiss et al., *Adv. Energy Mater.*, **11**, 2101126 (2021).
- S. Passerini, D. Bresser, A. Moretti, and A. Varzi, *Batteries: Present and Future Energy Storage Challenges* (Wiley-VCH Verlag, Weinheim, Germany) (2020), GmbH & Co. KGaA.
- T. Waldmann, S. Rössler, M. Blessing, R. Schäfer, R.-G. Scurtu, W. Braunwarth, and M. Wohlfahrt-Mehrens, *J. Electrochem. Soc.*, **168**, 90519 (2021).
- Y. Li and Y. Qi, *Energy Environ. Sci.*, **12**, 1286 (2019).
- K. G. Gallagher et al., *J. Electrochem. Soc.*, **163**, A138 (2016).
- L. S. Kremer, T. Danner, S. Hein, A. Hoffmann, B. Prifling, V. Schmidt, A. Latz, and M. Wohlfahrt-Mehrens, *Batteries & Supercaps*, **3**, 1172 (2020).
- Z. Du, D. L. Wood, C. Daniel, S. Kalnaus, and J. Li, *J. Appl. Electrochem.*, **47**, 405 (2017).
- L. Shen and Z. Chen, *Chem. Eng. Sci.*, **62**, 3748 (2007).
- J. Landesfeind, A. Ehrl, M. Graf, W. A. Wall, and H. A. Gasteiger, *J. Electrochem. Soc.*, **163**, A1254 (2016).
- M. Ebner and V. Wood, *J. Electrochem. Soc.*, **162**, A3064 (2015).
- C. Hogrefe, T. Waldmann, M. B. Molinero, L. Wildner, P. Axmann, and M. Wohlfahrt-Mehrens, *J. Electrochem. Soc.*, **169**, 50519 (2022).
- C. Hogrefe, T. Waldmann, M. Hölzle, and M. Wohlfahrt-Mehrens, *J. Power Sources*, **556**, 232391 (2023).
- D. S. Hall, A. Eldesoky, E. R. Logan, E. M. Tonita, X. Ma, and J. R. Dahn, *J. Electrochem. Soc.*, **165**, A2365 (2018).
- M. S. Ding, K. Xu, S. S. Zhang, K. Amine, G. L. Henriksen, and T. R. Jow, *J. Electrochem. Soc.*, **148**, A1196 (2001).
- Z. Du, D. L. Wood, and I. Belharouak, *Electrochem. Commun.*, **103**, 109 (2019).
- C. Mao, R. E. Ruther, J. Li, Z. Du, and I. Belharouak, *Electrochem. Commun.*, **97**, 37 (2018).
- N. Legrand, B. Knosp, P. Desprez, F. Lapique, and S. Raël, *J. Power Sources*, **245**, 208 (2014).
- T. Waldmann, B.-I. Hogg, M. Kasper, S. Grolleau, C. G. Couceiro, K. Trad, B. P. Matadi, and M. Wohlfahrt-Mehrens, *J. Electrochem. Soc.*, **163**, A1232 (2016).
- T. Waldmann, M. Wilka, M. Kasper, M. Fleischhammer, and M. Wohlfahrt-Mehrens, *J. Power Sources*, **262**, 129 (2014).
- J. C. Burns, D. A. Stevens, and J. R. Dahn, *J. Electrochem. Soc.*, **162**, A959 (2015).
- G. Kucinskis, M. Bozorgchenani, M. Feinauer, M. Kasper, M. Wohlfahrt-Mehrens, and T. Waldmann, *J. Power Sources*, **549**, 232129 (2022).
- J. Sturm, A. Frank, A. Rheinfeld, S. V. Erhard, and A. Jossen, *J. Electrochem. Soc.*, **167**, 130505 (2020).
- A. Frank, J. Sturm, M. Steinhardt, A. Rheinfeld, and A. Jossen, *ECS Adv.*, **1**, 40502 (2022).
- T. Waldmann, R.-G. Scurtu, D. Brändle, and M. Wohlfahrt-Mehrens, *Energy Technology*, **11**, 2200583 (2023).
- T. Waldmann, R.-G. Scurtu, D. Brändle, and M. Wohlfahrt-Mehrens, *Processes*, **9**, 1908 (2021).
- T. Ikeya et al., *J. Power Sources*, **75**, 101 (1998).
- T. Ikeya et al., *J. Power Sources*, **105**, 6 (2002).
- A. B. Khan and W. Choi, *IEEE Trans. Energy Convers.*, **33**, 1132 (2018).
- S. S. Zhang, *J. Power Sources*, **161**, 1385 (2006).
- J. Sieg, J. Bandlow, T. Mitsch, D. Dragicevic, T. Materna, B. Spier, H. Witzgenhausen, M. Ecker, and D. U. Sauer, *J. Power Sources*, **427**, 260 (2019).
- B.-I. Hogg, T. Waldmann, and M. Wohlfahrt-Mehrens, *J. Electrochem. Soc.*, **167**, 90525 (2020).
- T. Liu, X.-G. Yang, S. Ge, Y. Leng, and C.-Y. Wang, *eTransportation*, **7**, 100103 (2021).
- P. H. L. Notten, J. H. G. O. h Veld, and J. R. G. van Beek, *J. Power Sources*, **145**, 89 (2005).
- C. Chen, Z. Wei, and A. C. Knoll, *IEEE Trans. Transp. Electric.*, **8**, 3068 (2022).
- P. Keil and A. Jossen, *Journal of Energy Storage*, **6**, 125 (2016).
- J. Amanor-Boadu, A. Guiseppi-Elie, and E. Sánchez-Sinencio, *Energies*, **11**, 2162 (2018).
- N. Majid, S. Hafiz, S. Arianto, R. Y. Yuono, E. T. Astuti, and B. Prihandoko, *J. Phys. Conf. Ser.*, **817**, 12008 (2017).
- Y.-H. Liu and Y.-F. Luo, *IEEE Trans. Ind. Electron.*, **57**, 3963 (2010).
- X. Hu, Y. Zheng, X. Lin, and Y. Xie, *IEEE Trans. Transp. Electric.*, **6**, 427 (2020).
- I. A. Shkrob, M.-T. F. Rodrigues, and D. P. Abraham, *J. Electrochem. Soc.*, **168**, 10512 (2021).
- T. Waldmann, M. Kasper, and M. Wohlfahrt-Mehrens, *Electrochim. Acta*, **178**, 525 (2015).
- S. Radloff, G. Carbonari, R.-G. Scurtu, M. Hölzle, and M. Wohlfahrt-Mehrens, *J. Power Sources*, **553**, 232253 (2023).
- A. M. Colclasure, A. R. Dunlop, S. E. Trask, B. J. Polzin, A. N. Jansen, and K. Smith, *J. Electrochem. Soc.*, **166**, A1412 (2019).
- J. Steiger, D. Kramer, and R. Mönig, *Electrochim. Acta*, **136**, 529 (2014).
- X. Huang, *J. Solid State Electrochem.*, **15**, 649 (2011).
- B. Son, M.-H. Ryou, J. Choi, S.-H. Kim, J. M. Ko, and Y. M. Lee, *J. Power Sources*, **243**, 641 (2013).
- R. Raccichini, M. Amores, and G. Hinds, *Batteries*, **5**, 12 (2019).
- M. D. Levi, V. Dargel, Y. Shilina, D. Aurbach, and I. C. Halalay, *Electrochim. Acta*, **149**, 126 (2014).
- M.-T. F. Rodrigues, K. Kalaga, S. E. Trask, D. W. Dees, I. A. Shkrob, and D. P. Abraham, *J. Electrochem. Soc.*, **166**, A996 (2019).
- S. Tippmann, D. Walper, L. Balboa, B. Spier, and W. G. Bessler, *J. Power Sources*, **252**, 305 (2014).
- K.-H. Chen et al., *J. Power Sources*, **471**, 228475 (2020).
- S. Müller, J. Eller, M. Ebner, C. Burns, J. Dahn, and V. Wood, *J. Electrochem. Soc.*, **165**, A339 (2018).
- L. Hille, H.-C. Toepfer, C. Schriever, J. Kriegler, J. Keilhofer, M. P. Noecker, and M. F. Zaeh, *J. Electrochem. Soc.*, **169**, 60518 (2022).
- J. B. Hadedank, L. Kraft, A. Rheinfeld, C. Krezdorn, A. Jossen, and M. F. Zaeh, *J. Electrochem. Soc.*, **165**, A1563 (2018).
- L. Kraft, J. B. Hadedank, A. Frank, A. Rheinfeld, and A. Jossen, *J. Electrochem. Soc.*, **167**, 13506 (2020).
- J. Sandherr, S. Nester, M.-J. Kleefoot, M. Bolsinger, C. Weisenberger, A. Haghypour, D. K. Harrison, S. Ruck, H. Riegel, and V. Knoblauch, *J. Power Sources*, **549**, 232077 (2022).
- S. J. Harris, A. Timmons, D. R. Baker, and C. Monroe, *Chem. Phys. Lett.*, **485**, 265 (2010).
- V. A. Nalimova, D. Guérard, M. Lelaurain, and O. V. Fateev, *Carbon*, **33**, 177 (1995).
- K. C. Woo, W. A. Kamitakahara, D. P. DiVincenzo, D. S. Robinson, H. Mertwoy, J. W. Milliken, and J. E. Fischer, *Phys. Rev. Lett.*, **50**, 182 (1983).
- M. Tang, P. Albertus, and J. Newman, *Sol. State Ionics*, **156**, A390 (2009).
- M. Mancini, J. Martin, I. Ruggeri, N. Drewett, P. Axmann, and M. Wohlfahrt-Mehrens, *Batteries & Supercaps*, **5**, e202200109 (2022).
- I. Ruggeri, J. Martin, M. Wohlfahrt-Mehrens, and M. Mancini, *J. Solid State Electrochem.*, **26**, 73 (2022).
- J. Billaud, F. Bouville, T. Magrini, C. Villevieille, and A. R. Studart, *Nat. Energy*, **1**, 1 (2016).
- J.-H. Shim and S. Lee, *J. Power Sources*, **324**, 475 (2016).
- J. Kim, S. M. Nithya Jeghan, and G. Lee, *Microporous Mesoporous Mater.*, **305**, 110325 (2020).
- J. Remmlinger, S. Tippmann, M. Buchholz, and K. Dietmayer, *J. Power Sources*, **254**, 268 (2014).
- X.-G. Yang, T. Liu, Y. Gao, S. Ge, Y. Leng, D. Wang, and C.-Y. Wang, *Joule*, **3**, 3002 (2019).
- C.-Y. Wang, G. Zhang, S. Ge, T. Xu, Y. Ji, X.-G. Yang, and Y. Leng, *Nature*, **529**, 515 (2016).